

Ferromagnetism Mechanism in a Geometrically Frustrated Triangular Lattice

Qianqian Chen,¹ Shuai A. Chen,² and Zheng Zhu^{1,*}

¹Kavli Institute for Theoretical Sciences, University of Chinese Academy of Sciences, Beijing 100190, China

²Max Planck Institute for the Physics of Complex Systems, Nöthnitzer Straße 38, Dresden 01187, Germany

(Dated: August 13, 2024)

We study the emergent itinerant ferromagnetism and propose its underlying mechanism in the geometrically frustrated triangular lattice. Based on large-scale density matrix renormalization group simulations and unrestricted Hartree-Fock mean-field analysis, we identify itinerant ferromagnetic phases in the intermediate- U Hubbard model with finite doping and reveal the kinetic mechanisms assisted by geometric frustration. Notably, we find that the doublon-singlon exchange process among other microscopic charge hoppings solely drives the fully polarized ferromagnetism for geometrically frustrated triangular lattice. Additionally, we establish the whole magnetic phase diagram and illustrate itinerant ferromagnetism within a finite range of electron doping for finite on-site Coulomb repulsion. The comparison of local spin correlations with recent cold-atom experiments is also discussed. Our work enhances the understanding of ferromagnetism mechanisms at intermediate coupling strength and finite doping concentrations.

Introduction.—It has been a long-standing issue in physics to understand the ferromagnetism mechanism in strongly correlated systems. As the fundamental theoretical model for diverse physics of these systems, the Hubbard model [1–5] is initially formulated to understand the origin of ferromagnetism [6, 7]. The Hubbard Hamiltonian only includes the charge kinetic-energy term with the nearest-neighbor (NN) hopping amplitude t and on-site Coulomb repulsion U ,

$$H = -t \sum_{\langle ij \rangle, \sigma} \left(c_{i, \sigma}^\dagger c_{j, \sigma} + \text{H.c.} \right) + U \sum_{\mathbf{i}} n_{\mathbf{i}, \uparrow} n_{\mathbf{i}, \downarrow}. \quad (1)$$

Given the lack of explicit or effective magnetic interactions favoring ferromagnetic order, ferromagnetism can only arise from the delicate interplay between kinetic energy and on-site repulsion. To date, rigorous theoretical results on the ferromagnetism mechanism in the Hubbard model have only been achieved in specific limits [1–3]. The Stoner criterion [8] states that ferromagnetism occurs when the product of the density of states at the Fermi energy D_F and on-site Coulomb repulsion U satisfies the condition $UD_F > 1$. However, this criterion is derived from the Hartree-Fock approximation and is known to often overpredict ferromagnetic tendencies [3, 9]. Two other rigorous outcomes are Nagaoka ferromagnetism [10, 11], arising from kinetic energy minimization of a single doped hole at $U = \infty$, and flat-band ferromagnetism [12, 13] with dispersionless lowest energy bands. Over the past several decades, it has attracted substantial efforts to explore ferromagnetism beyond those well-known limits [14–34], particularly for the square lattices [14–17, 21, 22, 28, 29]. However, revealing the ferromagnetism mechanism in the ground state of geometrically frustrated triangular lattices at intermediate U and finite doping remains challenging [25, 32–34].

More recently, the realization of cold-atom quantum simulators of the triangular-lattice Hubbard model in optical lattices [35–38] has significantly advanced this issue. With unprecedented control over doping and coupling strength [39, 40], the ferromagnetic correlations are directly observed

[36–38] at intermediate on-site Coulomb repulsion and finite particle doping. In a different context, the transition metal dichalcogenides (TMD) moiré materials provide another avenue for simulating the triangular-lattice Hubbard model, wherein ferromagnetism has also been observed [41–44]. These experimental advancements necessitate theoretical study of the observed ferromagnetism and its microscopic mechanisms in the geometrically frustrated triangular lattice. Unlike the intensively studied hole-doped case, experimentally observed ferromagnetism occurs at the electron-doped side, the physics of which could be quite different due to the particle-hole asymmetry [36, 38, 45, 46]. In the limit of nearly half filling $n \rightarrow 1$ (n denotes electron density per site) and full filling $n \rightarrow 2$, the Nagaoka-type [20, 30, 31, 34, 46–48] and Müller-Hartmann-type ferromagnetism [49] have been proposed, respectively. However, the ferromagnetism mechanism for intermediate density around $n = 3/2$ is still an open issue. At $n = 3/2$, the Fermi surface nesting and van Hove singularities exist at $U = 0$, weak interactions would trigger instabilities towards magnetic orders with nesting wave vectors [50, 51]. However, when the weak-coupling theory fails at the strong-coupling regime [52], it is still a much-needed endeavor to identify the magnetism and its mechanism.

Motivated by the above, we explore the ferromagnetism and its underlying mechanism in the triangular-lattice Hubbard model from intermediate to infinite interactions near electron doping $\delta = 1/2$ (i.e., $n = 3/2$, where the doping concentration is defined by $\delta \equiv n - 1$). Using large-scale density matrix renormalization group (DMRG) and unrestricted Hartree-Fock (UHF) methods, we first present the emergence of ferromagnetic ground state with metallic charge behavior at $n = 3/2$ as the on-site Coulomb repulsion U increases from intermediate to strong and ultimately infinite values. By examining distinct microscopic hopping processes inherent in the Hubbard model at intermediate U , we reveal that the doublon-singlon exchange, assisted by the geometric frustration inherited from the lattice, solely contributes to the fully polarized ferromagnetism. We further confirm our conclusions by selectively deactivating each hopping process

and verifying their individual impacts on itinerant ferromagnetism. Additionally, we demonstrate that itinerant ferromagnetism around $\delta = 1/2$ persists within a specific range of electron doping and find the local spin correlations at zero temperature resemble those observed in a recent cold-atom experiment [36].

Itinerant Ferromagnetism at Electron Doping $\delta = 1/2$.— We first identify the nature of the ground state in the triangular-lattice Hubbard model at electron doping $\delta = 1/2$ using DMRG and UHF (details see supplementary [53]).

To examine the magnetic properties of the ground state, we use DMRG to compute the static spin structure factor $S(\mathbf{q})$, defined by $S(\mathbf{q}) \equiv \sum_{i,j} \langle \mathbf{S}_i \cdot \mathbf{S}_j \rangle e^{i\mathbf{q} \cdot (\mathbf{i}-\mathbf{j})} / N$. Magnetic order is signaled by peaks at certain wave vectors $\mathbf{q} = \mathbf{q}_0$. The DMRG simulations are performed on the cylinder with size $N = L_x \times L_y$, where L_x (L_y) represents the length of the cylinder (circumference). We mainly study $L_y = 4, 6$ and push bond dimension D up to $D \approx 36,000$. Notably, large bond dimensions are necessary for distinguishing ferromagnetic and incommensurate spin-density-wave (SDW) phases (see supplementary [53]). We first focus on the evolution of the momenta \mathbf{q}_0 as a function of interaction strength U/t . Our DMRG results reveal that, with increasing U/t , \mathbf{q}_0 progressively shifts from \mathbf{M} to Γ points [53] and finally fixed at the Γ beyond a critical strength U_c/t . We therefore keep track of the squared order parameter $m_s^2(\Gamma) \equiv S(\Gamma)/N$ as a function of U/t . As shown in Figs. 1(a), (c), when further increasing U/t , $m_s^2(\Gamma)$ gradually increases until plateauing, signaling the establishment of a stabilized ferromagnetic phase at larger U/t and the evolution from partially to fully polarized phases. The saturated value of $m_s^2(\Gamma)$ matches the theoretically expected $\delta_{\mathbf{q},\Gamma}/16$ at $n = 3/2$.

To confirm the robustness of ferromagnetism in the thermodynamic limit, we further employ the unrestricted Hartree-Fock (UHF) mean-field method [53]. In the UHF method, under an uncorrelated state ansatz, both the on-site densities $\langle n_{i,\sigma} \rangle$ and the spin-flips $\langle S_i^- \rangle$ and $\langle S_i^+ \rangle$ are involved to factorize the Hubbard interaction

$$n_{i,\uparrow} n_{i,\downarrow} \rightarrow \langle n_{i,\uparrow} \rangle n_{i,\downarrow} + \langle n_{i,\downarrow} \rangle n_{i,\uparrow} - \langle n_{i,\uparrow} \rangle \langle n_{i,\downarrow} \rangle - \langle S_i^+ \rangle S_i^- - \langle S_i^- \rangle S_i^+ + \langle S_i^- \rangle \langle S_i^+ \rangle. \quad (2)$$

Here $S_i^+ = c_{i,\uparrow}^\dagger c_{i,\downarrow}$ and $S_i^- = c_{i,\downarrow}^\dagger c_{i,\uparrow}$ are spin ladder operators. We have a total of $4N$ variational parameters, obtained through iterative diagonalization of the Hartree-Fock Hamiltonian. To ensure stable convergence, we utilize direct inversion in the iterative subspace method [54], and the convergence criterion for the energy is set to $10^{-8}t$. As shown in Fig. 1(b), the polarization $P \equiv 2Nm_s(\Gamma)$ increases gradually as U/t becomes larger, and finally a full polarization state occurs at $U \simeq 4.5t$ independently of system size. This aligns with Fig. 1(a) and is also consistent with the recent Hartree-Fock analysis [33], indicating robust fully-polarized ferromagnetism in the strong coupling regime.

Having established the ferromagnetism in the spin chan-

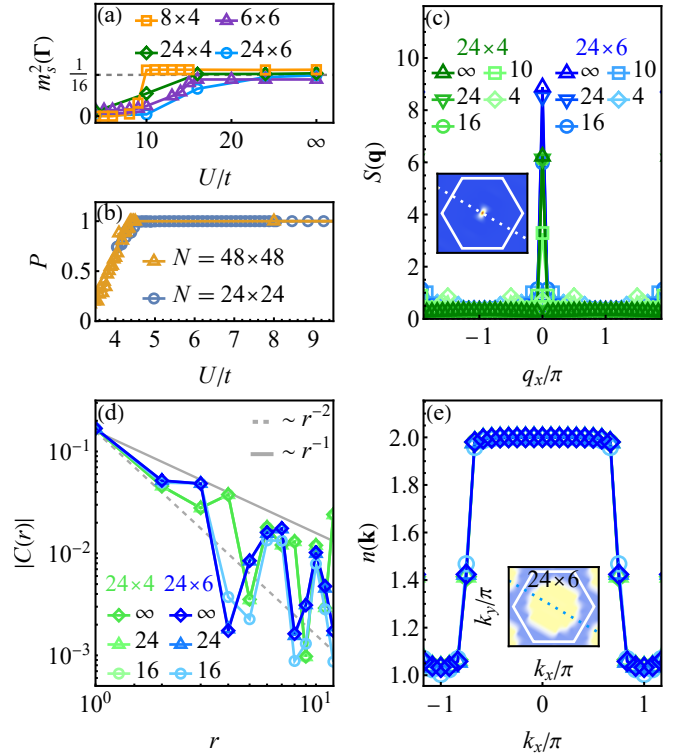


Fig. 1. Evolution of the magnetic and electronic structure across interaction U/t at electron doping $\delta = 1/2$. (a) Ferromagnetic squared order parameter $m_s^2(\Gamma)$ as a function of U/t . (b) Polarization P from unrestricted Hartree-Fock method with periodic boundary conditions. (c) Line-cut plot of the static spin structure factor $S(\mathbf{q})$ along momentum path through Γ point (white dashed line in inset). Labels are for different interactions U/t . (d) Single-particle propagator $|C(r)|$ for different U/t , compared to $\sim r^{-2}$ and $\sim r^{-1}$. (e) Line-cut plot of electron momentum distribution $n(\mathbf{k})$ along momentum path through the momentum Γ (blue dashed line in inset). Insets: contour plots of $S(\mathbf{q})$ in (c) and $n(\mathbf{k})$ in (e) with $U = 24$, $N = 24 \times 6$. White hexagon: the first Brillouin zone.

nel, we further examine the electronic properties in the charge channel. We compute the single-particle propagator $C(r) \equiv \sum_{\sigma} \langle c_{i_0,\sigma}^\dagger c_{i_0+r e_x,\sigma} \rangle$, and the momentum distribution of the electrons $n(\mathbf{k}) \equiv \sum_{i,j,\sigma} \langle c_{i,\sigma}^\dagger c_{j,\sigma} \rangle e^{i\mathbf{k} \cdot (\mathbf{i}-\mathbf{j})} / N$. Figure 1(d) illustrates the power-law decay of $|C(r)|$ with an exponent approximately equal to 1, identifying the gapless nature of the electrons in the ferromagnetic phase. In the inset of Fig. 1(e), the contour plot of $n(\mathbf{k})$ exhibits an abrupt change from 2 to 1 at certain momenta, as more clearly illustrated by the line-cut plot of $n(\mathbf{k})$ through the momentum Γ in the main panel of Fig. 1(e). This abrupt change indicates the presence of a well-defined Fermi surface, with the position of this sudden change characterizing the Fermi momenta. These observations are robust for the strength of intermediate-to-infinite interactions U/t and different system sizes N , suggesting that the electrons in the ferromagnetic phase for both intermediate U/t and infinite U/t limit are itinerant.

Kinetic Mechanism for Itinerant Ferromagnetism.— To

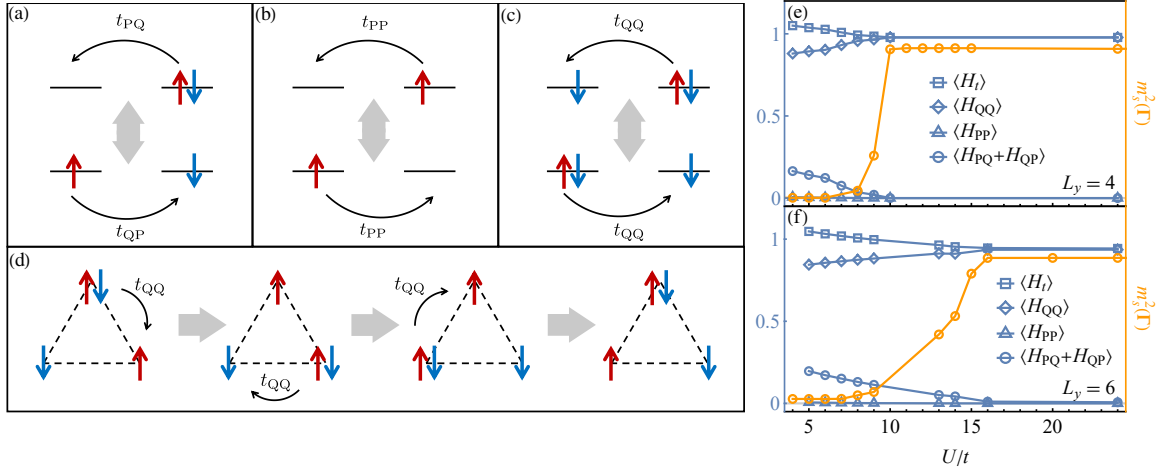


Fig. 2. Microscopic hopping processes in the Hubbard model and their kinetic energy contributions for intermediate U/t . (a)-(c) Schematic illustration of nearest-neighbor hopping processes between (a) a doubly occupied site and an empty site, or two singly occupied sites; (b) a singly occupied site and an empty site; (c) a doubly occupied site and a singly occupied site. These processes are described in (3). (d) Schematic illustration of ring-exchange coupling. (e),(f) The kinetic energies (in blue) of different microscopic hopping processes as functions of U/t for $L_y = 4$ in (e) and $L_y = 6$ in (f). Ferromagnetic squared order parameter $m_s^2(\Gamma)$ (in orange) is plotted for comparison.

understand the underlying mechanism for the itinerant ferromagnetism, we examine the distinct microscopic hopping processes encompassed in the hopping term H_t of the intermediate- U Hubbard model, as schematically illustrated in Figs. 2(a)-(c). Although all these hopping processes are allowed, whether ferromagnetism is induced specifically by a single process or several cooperative processes has yet to be conclusively established. We introduce the projection operator $\hat{Q}_{i,\sigma} \equiv n_{i,\sigma}$ and $\hat{P}_{i,\sigma} \equiv 1 - \hat{Q}_{i,\sigma}$ to decompose the hopping term H_t :

$$\begin{aligned}
 H_t = & - \sum_{\langle ij \rangle, \sigma} (t_{PQ} \hat{P}_{i,\bar{\sigma}} c_{i,\sigma}^\dagger c_{j,\sigma} \hat{Q}_{j,\bar{\sigma}} + t_{QP} \hat{Q}_{i,\bar{\sigma}} c_{i,\sigma}^\dagger c_{j,\sigma} \hat{P}_{j,\bar{\sigma}} \\
 & + t_{PP} \hat{P}_{i,\bar{\sigma}} c_{i,\sigma}^\dagger c_{j,\sigma} \hat{P}_{j,\bar{\sigma}} + t_{QQ} \hat{Q}_{i,\bar{\sigma}} c_{i,\sigma}^\dagger c_{j,\sigma} \hat{Q}_{j,\bar{\sigma}} + \text{H.c.}) \quad (3) \\
 \equiv & - \sum_{\langle ij \rangle, \sigma} [t_{PQ}(H_{PQ} + H_{QP}) + t_{PP}H_{PP} + t_{QQ}H_{QQ}].
 \end{aligned}$$

Consequently, H_t includes NN hopping between (i) a doubly occupied site and an empty site with hopping amplitude t_{PQ} , or two singly occupied sites with hopping amplitude t_{QP} [see Fig. 2(a)]; (ii) a singly occupied site and an empty site with hopping amplitude t_{PP} [see Fig. 2(b)], i.e., singlon hopping; (iii) a doubly occupied and a singly occupied site with hopping amplitude t_{QQ} [see Fig. 2(c)], i.e., the doublon-singlon exchange. Given that case (i) describes Hermitian conjugate processes for an isotropic case, we consider $t_{PQ} = t_{QP}$. The hopping term in the Hubbard model (S1) corresponds to the isotropic limit $t_{PQ} = t_{QP} = t_{PP} = t_{QQ} = t$. This decomposition enables us to examine the individual contributions of each microscopic hopping to itinerant ferromagnetism.

As shown in Figs. 2(e-f) for $L_y = 4, 6$ DMRG cylinders, before entering the fully polarized region where $m_s^2(\Gamma)$ saturates, multiple hopping processes have nonzero expectation

values, suggesting that all contribute to the ground-state kinetic energy. In contrast, when increasing U/t , only $\langle H_{QQ} \rangle$ is nonzero in the fully polarized region. This observation strongly suggests that, among distinct hopping processes, the doublon-singlon exchange uniquely drives the fully polarized ferromagnetism. Then we focus on this hopping process and further analyze the role of lattice geometric frustration in resulting ferromagnetism.

The effective NN spin interactions $\mathbf{S}_i \cdot \mathbf{S}_j$ stems from two kinds of virtual hopping processes at finite electron doping: (i) the superexchange t^2/U favoring antiferromagnetic order, (ii) the doublon-assisted ring-exchange t^3/V^2 [see Fig. 2(d)] favoring either antiferromagnetic or ferromagnetic order depending on the sign of hopping t [1, 10], where V refers to the on-site potential pinning the doublon. Therefore, the effective spin interaction is $\sim \lim_{V \rightarrow 0} (t^2/U + t^3/V^2) \mathbf{S}_i \cdot \mathbf{S}_j$. This formulation reveals a fundamental difference between hole and electron doping in triangular lattices. For hole-doping ($t > 0$), both hopping processes favor antiferromagnetism; while for electron-doping ($t < 0$), the ring-exchange virtual process promotes ferromagnetism and finally dominates over the superexchange coupling in the large and infinite U limit. Notably, square lattices lack such particle-hole asymmetry due to the positive ring-exchange coupling $\sim t^4$. This distinction highlights the important properties of geometrically frustrated lattices like the triangular lattice, where kinetic energy and geometric frustration work synergistically to foster itinerant ferromagnetism.

To further verify the unique role of the doublon-singlon exchange in driving ferromagnetism, we independently deactivate each hopping amplitude while keeping the others unchanged, and compare the resulting ground states with the standard Hubbard model (S1). Therefore, the specific hop-

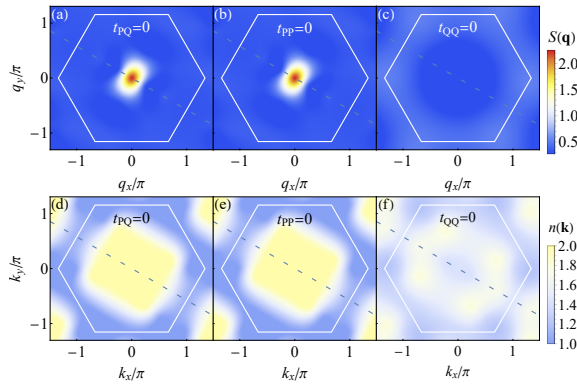


Fig. 3. Impact of the microscopic hopping processes on itinerant ferromagnetism in the Hubbard model. (a)-(f) Static spin structure factor $S(\mathbf{q})$ ((a)-(c)) and the momentum distribution $n(\mathbf{k})$ ((d)-(f)) obtained by independently turning off each hopping process: (a),(d) $t_{PQ} = 0$, (b),(e), $t_{PP} = 0$, (c),(f), $t_{QQ} = 0$. Other hopping terms in (3) are set to t . The white hexagon indicates the first Brillouin zone; interpolation is applied to contours.

ping process whose deactivation eliminates itinerant ferromagnetism is crucial for ferromagnetism. Figures 3 reveal that only switching off t_{PQ} or t_{PP} does not significantly affect the ferromagnetism, as the resulting $S(\mathbf{q})$ [see Figs. 3(a),(b)] and $n(\mathbf{k})$ [see Figs. 3(d),(e)] remain similar to those of the Hubbard model (S1) [see Figs. 1(c),(e)]. Conversely, switching off t_{QQ} eliminates ferromagnetic signatures [Figs. 3(c),(f)], since both the characteristic peak in $S(\mathbf{q})$ and well-defined Fermi surface in $n(\mathbf{k})$ disappear. These numerical results suggest the microscopic hopping process H_{QQ} , as illustrated in Fig. 2(c), is pivotal in driving ferromagnetism at finite U . We further confirm this conclusion by examining a $t_{QQ}-U$ model with only $t_{QQ} = t$ and finite U while $t_{PQ} = t_{QP} = t_{PP} = 0$, and the itinerant ferromagnetism is observed (details see Supplementary[53]).

Evolution of Magnetism with Doping.— Below, we explore magnetism with a broader doping range. We examine both the local and global spin correlations through the NN spin correlations and the static spin structure factors, respectively.

The average local spin correlations are defined as $\bar{S}(r) = \frac{1}{z} \sum_{\mathbf{j}, |\mathbf{i}_0 - \mathbf{j}| = r} \langle \mathbf{S}_{\mathbf{i}_0} \cdot \mathbf{S}_{\mathbf{j}} \rangle$, with the summation over neighbors at a distance r from a fixed site \mathbf{i}_0 that is strategically positioned at the lattice's center to avoid a boundary effect. Here, we consider $r = 1$ for NN spin correlations, and $z = 6$ represents the coordination number of the triangular lattice. As shown in Fig. 4(a), the average NN correlations are antiferromagnetic across a broad range of hole doping ($\delta < 0$) at intermediate coupling strength $U/t = 10$, yet they are markedly suppressed by electron doping ($\delta > 0$). In particular, we observe that the local spin correlations become ferromagnetic at intermediate electron doping. Notably, these local spin correlations at zero temperature align well with the recent cold-atom experimental findings (Fig. 3b of Ref. [36]) at finite temperature for the similar intermediate U/t . This observation suggests that the

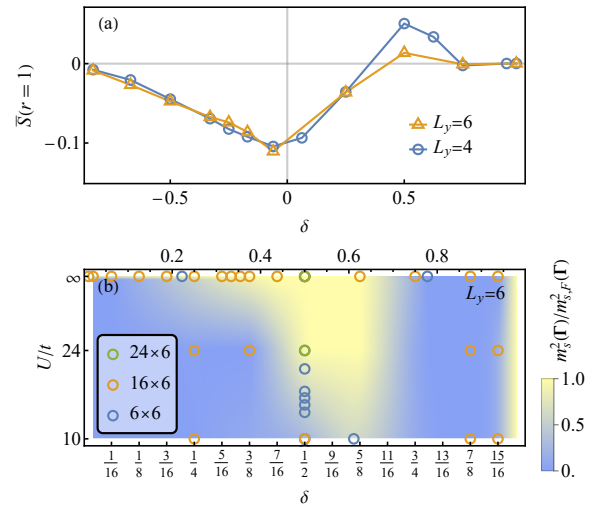


Fig. 4. Phase diagram. (a) Average NN spin correlations $\bar{S}(r = 1)$ as a function of doping δ on width $L_y = 4, 6$ cylinders, resembling cold-atom quantum simulator findings [36] for the same model. (b) Renormalized ferromagnetic order parameter $m_s^2(\Gamma)/m_{s,F}^2(\Gamma)$ for the Hubbard model (S1) as a function of doping δ and interaction U/t . $m_{s,F}^2(\Gamma) \equiv [(1 - \delta)/2]^2$ is full polarization value of $m_s^2(\Gamma)$. Circles denote the data obtained numerically.

local magnetic properties of the ground state survive in a finite range of temperatures.

We further examine the static spin structure factors to establish the magnetic phase diagram as a function of interaction U/t and electron doping $\delta > 0$. As illustrated in Fig.4(b) for $L_y = 6$ cylinders, the renormalized squared order parameter $m_s^2(\Gamma)/m_{s,F}^2(\Gamma)$ shows ferromagnetism in a finite range of dopings $\delta \approx 1/2$ and interactions $U \gtrsim 10$, which smoothly extends to the infinite interaction limit. These findings are consistent with $L_y = 4$ cylinders [53]. Together with the numerical evidence presented in the previous section, this demonstrates that the ferromagnetism at both finite and infinite U around $\delta \approx 1/2$ is driven by the doublon-singlon exchange.

Moreover, for finite U and dopings both below and above $\delta \approx 1/2$, the incommensurate spin density wave (iSDW) emerges [53] for both $L_y = 4$ and $L_y = 6$, which separates the ferromagnetic phase at $n = 3/2$ from the phases near the full-filling and half-filling limits. We remark that, unlike the consistent observations at finite coupling strength, at $U = \infty$, we find a smooth connection between the ferromagnetic phase at $\delta \gtrsim 0$ and $\delta \approx 1/2$ when $L_y = 6$, but these two phases are separated by an iSDW phase when $L_y = 4$ [53]. In addition, for larger doping $5/8 \lesssim \delta < 1$, both $L_y = 4$ and $L_y = 6$ systems exhibit another iSDW phase [see supplementary[53]], separating the ferromagnetic regions observed at $\delta \approx 1/2$ from ferromagnetism at $\delta \rightarrow 1$, thus suggesting distinct underlying mechanisms in these two doping concentrations.

Summary and outlook.— In this work, we explore the ferromagnetism mechanism of the finite-doped triangular-lattice

Hubbard model at intermediate on-site Coulomb interaction. By diagnosing each microscopic hopping process separately, we reveal that the geometrically frustrated doublon-singlon exchange among other hopping processes in triangular lattices solely contributes to the fully polarized ferromagnetism. We further establish the magnetic phase diagram for the electron-doped triangular Hubbard model and compare the local spin correlations with the latest cold-atom experiments. Our findings may stimulate future studies of the triangular-lattice ferromagnetism beyond the cold-atom systems, particularly in condensed matter physics. For instance, the TMD moiré materials offer platforms with additional tuning parameters to study the stability of ferromagnetism against long-range Coulomb interactions in TMD hetero-bilayers [55–59] and complex hopping in TMD homo-bilayers [60]. It may also inspire future finite-temperature numerical works to understand the relationship between rising temperature and increasing coupling strength, as previously focused on the half-filling case [61, 62].

We particularly thank helpful discussions with Ashvin Vishwanath. This work is supported by the National Natural Science Foundation of China (Grant No.12074375), the Fundamental Research Funds for the Central Universities and the Strategic Priority Research Program of CAS (Grant No.XDB33000000).

* zhuzheng@ucas.ac.cn

- [1] H. Tasaki, The Hubbard model - an introduction and selected rigorous results, *Journal of Physics: Condensed Matter* **10**, 4353 (1998).
- [2] H. Tasaki, From Nagaoka's Ferromagnetism to Flat-Band Ferromagnetism and Beyond: An Introduction to Ferromagnetism in the Hubbard Model, *Progress of Theoretical Physics* **99**, 489 (1998).
- [3] D. Vollhardt, N. Blümer, K. Held, M. Kollar, J. Schlipf, M. Ulmke, and J. Wahle, Metallic ferromagnetism: Progress in our understanding of an old strong-coupling problem, in *Advances in Solid State Physics* **38**, edited by B. Kramer (Springer Berlin Heidelberg, Berlin, Heidelberg, 1999) pp. 383–396.
- [4] D. P. Arovas, E. Berg, S. A. Kivelson, and S. Raghu, The hubbard model, *Annual Review of Condensed Matter Physics* **13**, 239 (2022).
- [5] M. Qin, T. Schäfer, S. Andergassen, P. Corboz, and E. Gull, The Hubbard Model: A Computational Perspective, *Annual Review of Condensed Matter Physics* **13**, 275 (2022).
- [6] M. C. Gutzwiller, Effect of Correlation on the Ferromagnetism of Transition Metals, *Phys. Rev. Lett.* **10**, 159 (1963).
- [7] J. Hubbard and B. H. Flowers, Electron correlations in narrow energy bands, *Proceedings of the Royal Society of London. Series A. Mathematical and Physical Sciences* **276**, 238 (1963).
- [8] E. C. Stoner, Collective electron ferromagnetism, *Proceedings of the Royal Society of London. Series A. Mathematical and Physical Sciences* **165**, 372 (1938).
- [9] D. Vollhardt, N. Blümer, K. Held, M. Kollar, J. Schlipf, and M. Ulmke, Non-perturbative approaches to magnetism in strongly correlated electron systems, *Zeitschrift für Physik B Condensed Matter* **103**, 283 (1996).
- [10] D. J. Thouless, Exchange in solid ^3He and the Heisenberg Hamiltonian, *Proceedings of the Physical Society* **86**, 893 (1965).
- [11] Y. Nagaoka, Ferromagnetism in a Narrow, Almost Half-Filled s Band, *Phys. Rev.* **147**, 392 (1966).
- [12] A. Mielke, Ferromagnetism in the Hubbard model on line graphs and further considerations, *Journal of Physics A: Mathematical and General* **24**, 3311 (1991).
- [13] H. Tasaki, Ferromagnetism in the hubbard models with degenerate single-electron ground states, *Phys. Rev. Lett.* **69**, 1608 (1992).
- [14] J. A. Riera and A. P. Young, Ferromagnetism in the one-band hubbard model, *Phys. Rev. B* **40**, 5285 (1989).
- [15] A. G. Basile and V. Elser, Stability of the ferromagnetic state with respect to a single spin flip: Variational calculations for the $u=\infty$ hubbard model on the square lattice, *Phys. Rev. B* **41**, 4842 (1990).
- [16] V. J. Emery, S. A. Kivelson, and H. Q. Lin, Phase separation in the t-J model, *Phys. Rev. Lett.* **64**, 475 (1990).
- [17] B. S. Shastry, H. R. Krishnamurthy, and P. W. Anderson, Instability of the nagaoka ferromagnetic state of the $u=\infty$ hubbard model, *Phys. Rev. B* **41**, 2375 (1990).
- [18] A. Mielke, Ferromagnetic ground states for the hubbard model on line graphs, *Journal of Physics A: Mathematical and General* **24**, L73 (1991).
- [19] A. Mielke, Exact ground states for the Hubbard model on the Kagome lattice, *Journal of Physics A: Mathematical and General* **25**, 4335 (1992).
- [20] T. Hanisch, B. Kleine, A. Ritzl, and E. Müller-Hartmann, Ferromagnetism in the Hubbard model: instability of the Nagaoka state on the triangular, honeycomb and kagome lattices, *Annalen der Physik* **507**, 303 (1995).
- [21] P. Wurth, G. Uhrig, and E. Müller-Hartmann, Ferromagnetism in the Hubbard model on the square lattice: Improved instability criterion for the Nagaoka state, *Annalen der Physik* **508**, 148 (1996).
- [22] M. Brunner and A. Muramatsu, Quantum monte carlo simulations of infinitely strongly correlated fermions, *Phys. Rev. B* **58**, R10100 (1998).
- [23] M. Ulmke, Ferromagnetism in the hubbard model on fcc-type lattices, *The European Physical Journal B-Condensed Matter and Complex Systems* **1**, 301 (1998).
- [24] F. Becca and S. Sorella, Nagaoka ferromagnetism in the two-dimensional infinite- U hubbard model, *Phys. Rev. Lett.* **86**, 3396 (2001).
- [25] J. Merino, B. J. Powell, and R. H. McKenzie, Ferromagnetism, paramagnetism, and a Curie-Weiss metal in an electron-doped Hubbard model on a triangular lattice, *Phys. Rev. B* **73**, 235107 (2006).
- [26] C.-C. Chang, S. Zhang, and D. M. Ceperley, Itinerant ferromagnetism in a fermi gas with contact interaction: Magnetic properties in a dilute hubbard model, *Phys. Rev. A* **82**, 061603 (2010).
- [27] S.-Y. Chang, M. Randeria, and N. Trivedi, Ferromagnetism in the upper branch of the Feshbach resonance and the hard-sphere Fermi gas, *Proceedings of the National Academy of Sciences* **108**, 51 (2011).
- [28] G. Carleo, S. Moroni, F. Becca, and S. Baroni, Itinerant ferromagnetic phase of the hubbard model, *Phys. Rev. B* **83**, 060411 (2011).
- [29] L. Liu, H. Yao, E. Berg, S. R. White, and S. A. Kivelson, Phases of the Infinite U Hubbard Model on Square Lattices, *Phys. Rev. Lett.* **108**, 126406 (2012).
- [30] H. Schlömer, U. Schollwöck, A. Bohrdt, and F. Grusdt, Kinetic-

- to-magnetic frustration crossover and linear confinement in the doped triangular $t - J$ model (2023), [arXiv:2305.02342 \[cond-mat.str-el\]](#).
- [31] M. Davydova, Y. Zhang, and L. Fu, Itinerant spin polaron and metallic ferromagnetism in semiconductor moiré superlattices, *Phys. Rev. B* **107**, 224420 (2023).
- [32] R. Samajdar and R. N. Bhatt, Nagaoka ferromagnetism in doped hubbard models in optical lattices (2023), [arXiv:2305.05683 \[cond-mat.str-el\]](#).
- [33] Y. He, R. Rausch, M. Peschke, C. Karrasch, P. Corboz, N. Bulfinch, and S. A. Parameswaran, Itinerant Magnetism in the Triangular Lattice Hubbard Model at Half-doping: Application to Twisted Transition-Metal Dichalcogenides (2023), [arXiv:2311.10146 \[cond-mat.str-el\]](#).
- [34] I. Morera and E. Demler, Itinerant magnetism and magnetic polarons in the triangular lattice Hubbard model (2024), [arXiv:2402.14074 \[cond-mat.str-el\]](#).
- [35] J. Yang, L. Liu, J. Mongkolkiattichai, and P. Schauss, Site-resolved imaging of ultracold fermions in a triangular-lattice quantum gas microscope, *PRX Quantum* **2**, 020344 (2021).
- [36] M. Xu, L. H. Kendrick, A. Kale, Y. Gang, G. Ji, R. T. Scalettar, M. Lebrat, and M. Greiner, Frustration-and doping-induced magnetism in a fermi-hubbard simulator, *Nature* **620**, 971 (2023).
- [37] M. Lebrat, M. Xu, L. H. Kendrick, A. Kale, Y. Gang, P. Seetharaman, I. Morera, E. Khatami, E. Demler, and M. Greiner, Observation of nagaoka polarons in a fermi-hubbard quantum simulator, *Nature* **629**, 317 (2024).
- [38] M. L. Prichard, B. M. Spar, I. Morera, E. Demler, Z. Z. Yan, and W. S. Bakr, Directly imaging spin polarons in a kinetically frustrated hubbard system, *Nature* **629**, 323 (2024).
- [39] C. Chin, R. Grimm, P. Julienne, and E. Tiesinga, Feshbach resonances in ultracold gases, *Rev. Mod. Phys.* **82**, 1225 (2010).
- [40] M. Lewenstein, A. Sanpera, and V. Ahufinger, *Ultracold Atoms in Optical Lattices: Simulating quantum many-body systems* (Oxford University Press, 2012).
- [41] Y. Tang, L. Li, T. Li, Y. Xu, S. Liu, K. Barmak, K. Watanabe, T. Taniguchi, A. H. MacDonald, J. Shan, *et al.*, Simulation of Hubbard model physics in WSe₂/WS₂ moiré superlattices, *Nature* **579**, 353 (2020).
- [42] L. Ciorciaro, T. Smoleński, I. Morera, N. Kiper, S. Hiestand, M. Kroner, Y. Zhang, K. Watanabe, T. Taniguchi, E. Demler, *et al.*, Kinetic magnetism in triangular moiré materials, *Nature* **623**, 509 (2023).
- [43] E. Anderson, F.-R. Fan, J. Cai, W. Holtzmann, T. Taniguchi, K. Watanabe, D. Xiao, W. Yao, and X. Xu, Programming correlated magnetic states with gate-controlled moiré geometry, *Science* **381**, 325 (2023).
- [44] U. F. P. Seifert and L. Balents, Spin polarons and ferromagnetism in doped dilute moiré-mott insulators, *Phys. Rev. Lett.* **132**, 046501 (2024).
- [45] Z. Zhu and Q. Chen, Superconductivity in doped triangular mott insulators: The roles of parent spin backgrounds and charge kinetic energy, *Phys. Rev. B* **107**, L220502 (2023).
- [46] S. A. Chen, Q. Chen, and Z. Zhu, Proposal for asymmetric photoemission and tunneling spectroscopies in quantum simulators of the triangular-lattice Fermi-Hubbard model, *Phys. Rev. B* **106**, 085138 (2022).
- [47] I. Morera, M. Kanász-Nagy, T. Smolenski, L. Ciorciaro, A. m. c. Imamoğlu, and E. Demler, High-temperature kinetic magnetism in triangular lattices, *Phys. Rev. Res.* **5**, L022048 (2023).
- [48] K. Lee, P. Sharma, O. Vafek, and H. J. Changlani, Triangular lattice hubbard model physics at intermediate temperatures, *Phys. Rev. B* **107**, 235105 (2023).
- [49] C. Li, M.-G. He, C.-Y. Wang, and H. Zhai, Frustration induced Itinerant Ferromagnetism of Fermions in Optical Lattice (2023), [arXiv:2305.01682 \[cond-mat.quant-gas\]](#).
- [50] I. Martin and C. D. Batista, Itinerant Electron-Driven Chiral Magnetic Ordering and Spontaneous Quantum Hall Effect in Triangular Lattice Models, *Phys. Rev. Lett.* **101**, 156402 (2008).
- [51] Y. Akagi and Y. Motome, Spin Chirality Ordering and Anomalous Hall Effect in the Ferromagnetic Kondo Lattice Model on a Triangular Lattice, *Journal of the Physical Society of Japan* **79**, 083711 (2010).
- [52] K. Pasrija and S. Kumar, Noncollinear and noncoplanar magnetic order in the extended hubbard model on anisotropic triangular lattice, *Phys. Rev. B* **93**, 195110 (2016).
- [53] Further details are available as supplementary material.
- [54] P. Pulay, Convergence acceleration of iterative sequences. the case of scf iteration, *Chemical Physics Letters* **73**, 393 (1980).
- [55] C. Jin, Z. Tao, T. Li, Y. Xu, Y. Tang, J. Zhu, S. Liu, K. Watanabe, T. Taniguchi, J. C. Hone, *et al.*, Stripe phases in WSe₂/WS₂ moiré superlattices, *Nature Materials* **20**, 940 (2021).
- [56] Y. Xu, S. Liu, D. A. Rhodes, K. Watanabe, T. Taniguchi, J. Hone, V. Elser, K. F. Mak, and J. Shan, Correlated insulating states at fractional fillings of moiré superlattices, *Nature* **587**, 214 (2020).
- [57] T. Senthil, A. Vishwanath, L. Balents, S. Sachdev, and M. P. A. Fisher, Deconfined Quantum Critical Points, *Science* **303**, 1490 (2004).
- [58] T. Senthil, L. Balents, S. Sachdev, A. Vishwanath, and M. P. A. Fisher, Quantum criticality beyond the Landau-Ginzburg-Wilson paradigm, *Phys. Rev. B* **70**, 144407 (2004).
- [59] T. Senthil, Deconfined quantum critical points: a review (2023), [arXiv:2306.12638 \[cond-mat.str-el\]](#).
- [60] L. Wang, E.-M. Shih, A. Ghiotto, L. Xian, D. A. Rhodes, C. Tan, M. Claassen, D. M. Kennes, Y. Bai, B. Kim, *et al.*, Correlated electronic phases in twisted bilayer transition metal dichalcogenides, *Nature materials* **19**, 861 (2020).
- [61] A. Wietek, R. Rossi, F. Šimkovic, M. Klett, P. Hansmann, M. Ferrero, E. M. Stoudenmire, T. Schäfer, and A. Georges, Mott Insulating States with Competing Orders in the Triangular Lattice Hubbard Model, *Phys. Rev. X* **11**, 041013 (2021).
- [62] M. Zhang, X. Zhao, K. Watanabe, T. Taniguchi, Z. Zhu, F. Wu, Y. Li, and Y. Xu, Tuning Quantum Phase Transitions at Half Filling in 3L-MoTe₂/WSe₂ Moiré Superlattices, *Phys. Rev. X* **12**, 041015 (2022).

Supplementary Materials for “Ferromagnetism Mechanism in a Geometrically Frustrated Triangular Lattice”

DMRG DETAILS AND DMRG CONVERGENCE

In this section, we provide more numerical details in our calculations, as well as DMRG convergence with bond dimension. We study the ground-state properties of the triangular-lattice Hubbard model using DMRG. The Hamiltonian reads

$$H = -t \sum_{\langle ij \rangle, \sigma} \left(c_{i, \sigma}^\dagger c_{j, \sigma} + \text{H.c.} \right) + U \sum_{\mathbf{i}} n_{i, \uparrow} n_{i, \downarrow}. \quad (\text{S1})$$

Here, $t > 0$ and $U > 0$ are the nearest-neighbor (NN) hopping amplitude and the on-site Coulomb repulsion energies. The operators $c_{i, \sigma}^{(\dagger)}$ ($c_{i, \sigma}$) creates (annihilates) an electron on site \mathbf{i} with spin $\sigma = \uparrow, \downarrow$, and $n_{i, \sigma} \equiv c_{i, \sigma}^\dagger c_{i, \sigma}$ is the number operator. The summation of bonds $\langle \dots \rangle$ runs over all NN bonds in the triangular lattice. The doping concentration is represented by $\delta = n - 1$, with n indicating the electron density per site. Here, $\delta = 0$ corresponds to the half-filling, and $\delta > 0$ ($\delta < 0$) is the electron-doped (hole-doped) case.

We employ DMRG to simulate the Hamiltonian in Eq. (S1) on triangular lattice cylinders with primitive vectors $\mathbf{e}_x = (1, 0)$, $\mathbf{e}_y = (1/2, \sqrt{3}/2)$, wrapping on cylinders with a lattice spacing of unity. System size is $N = L_x \times L_y$, where L_x (L_y) represents the length of the cylinder (circumference). Here we mainly study cylinders with width $L_y = 4, 6$ and set the energy unit as t . In particular, we extend our computation from finite- U to the infinite- U limit using the effective t - J model with vanishing superexchange interaction $J = 4t^2/U$. Considering the varying convergence rates at different parameters, we set the DMRG bond dimension D up to $D \approx 36,000$.

We provide specific examples to illustrate the necessity of large bond dimensions for accurately identifying the ground-state properties of both the ferromagnetic phase and incommensurate SDW phases. Additionally, we have performed DMRG calculations with different initial states to ensure the convergence of DMRG.

For incommensurate SDW region, at relatively small bond dimensions, the peak of the static spin structure $S(\mathbf{q})$ is located at the momentum Γ [see Fig. S1(a,c,d)], which is a signature for ferromagnetism. However, with the increase of bond dimension, the energy becomes lower and the peak splits around the momentum Γ . These observations indicate large bond dimensions are required to obtain converged results for distinguishing the ferromagnetism and iSDW with close energies.

On the other side, for the ferromagnetism region, a large bond dimension is crucial for determining whether the ground state is partially polarized or fully polarized. As presented in Fig. S1(b), the peak of $S(\mathbf{q})$ gets higher with increasing bond dimension, until it saturates. Notably, DMRG convergence becomes more challenging with decreasing interaction strength U/t and increasing system size N . In Fig. S1(f,e), we also present the good convergence of the DMRG simulations in the iSDW region at $U = \infty$ that separates the ferromagnetic phases at $\delta \approx 1/16$ and $\delta \approx 1/2$ [see Fig. S6(b)].

DETAILS ON UNRESTRICTED HARTREE-FOCK METHOD

We consider the Hubbard model on the triangular lattice with the Hamiltonian

$$H = - \sum_{\langle ij \rangle, \sigma} (t + \mu \delta_{ij}) c_{i, \sigma}^\dagger c_{j, \sigma} + U \sum_{\mathbf{i}} n_{i, \uparrow} n_{i, \downarrow} \quad (\text{S2})$$

Here t is the hopping integral and U is the on-site Hubbard interaction strength. Our focus is on a scenario of high electron doping $\delta = 0.5$ and applying the unrestricted Hartree-Fock (UHF) approximation. In the UHF approximation, the mean-field order parameters are introduced for both the on-site densities $\langle n_{i, \sigma} \rangle$ and the spin-flips $\langle S_i^- \rangle$ and $\langle S_i^+ \rangle$. Then, the Hartree-Fock factorizes the Hamiltonian to

$$H_{\text{HF}} = - \sum_{\langle ij \rangle} (t + \mu \delta_{ij}) c_{i, \sigma}^\dagger c_{j, \sigma} + \sum_{\mathbf{i}} U [\langle n_{i, \uparrow} \rangle n_{i, \downarrow} + \langle n_{i, \downarrow} \rangle n_{i, \uparrow} - \langle S_i^+ \rangle S_i^- - \langle S_i^- \rangle S_i^+] + \sum_{\mathbf{i}} U [-\langle n_{i, \uparrow} \rangle \langle n_{i, \downarrow} \rangle + \langle S_i^- \rangle \langle S_i^+ \rangle],$$

Here the mean-field parameters is an expectation value under the ground state $|\text{HF}\rangle$ of the H_{HF} mean-field Hamiltonian,

$$\langle n_{i, \sigma} \rangle \equiv \langle \text{HF} | n_{i, \sigma} | \text{HF} \rangle, \quad \langle S_i^\pm \rangle \equiv \langle \text{HF} | S_i^\pm | \text{HF} \rangle, \quad (\text{S3})$$

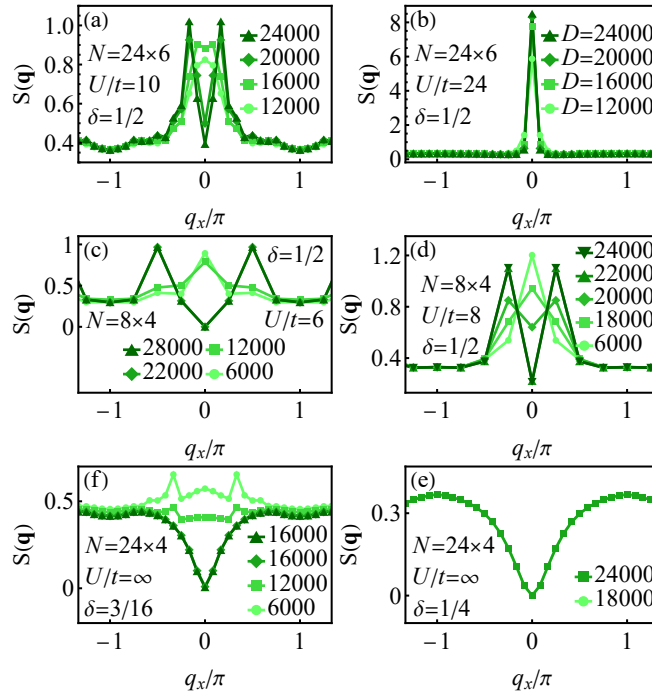


Fig. S1. Line-cut plot of the static spin structure $S(\mathbf{q})$ along the momentum path passing through the Γ point (denoted as the white dashed line in Fig. 1(c) in the main text) with respect to various bond dimensions D .

and the on-site densities are subject to the particle number constraint $\sum_{\mathbf{i}}[\langle n_{\mathbf{i},\uparrow} \rangle + \langle n_{\mathbf{i},\downarrow} \rangle] = N(1 + \delta)$, with N being the number of the lattice sites. We have total $4N$ variational parameters, which can be iteratively solved by the self-consistent equations

$$\langle n_{\mathbf{i},\sigma} \rangle = \sum_n f_{FD}(E_n) \langle \psi_n | n_{\mathbf{i},\sigma} | \psi_n \rangle \quad (\text{S4})$$

$$\langle S_{\mathbf{i}}^{\pm} \rangle = \sum_n f_{FD}(E_n) \langle \psi_n | S_{\mathbf{i}}^{\pm} | \psi_n \rangle \quad (\text{S5})$$

where $|\psi_n\rangle$ is an eigenstate of H_{HF} with $H_{\text{HF}}|\psi_n\rangle = E_n|\psi_n\rangle$ and $f_{FD}(E_n)$ is the Fermi-Dirac distribution.

For a stable convergence, we utilize the direct inversion in the iterative subspace (DIIS) method. In this approach, we can express the Hartree-Fock Hamiltonian in matrix form as follows:

$$H_{\text{HF}} = C^{\dagger} F C + \sum_{\mathbf{i}} U [-\langle n_{\mathbf{i},\uparrow} \rangle \langle n_{\mathbf{i},\downarrow} \rangle + \langle S_{\mathbf{i}}^{-} \rangle \langle S_{\mathbf{i}}^{+} \rangle] \quad (\text{S6})$$

where C is a vector with $C_{\mathbf{i}\sigma} = c_{\mathbf{i},\sigma}$ and F is the Fock matrix. For the magnetic order, the single-particle correlation matrix Φ is defined as

$$\Phi_{\mathbf{ij},\alpha\beta} = \langle c_{\mathbf{i},\alpha}^{\dagger} c_{\mathbf{j},\beta} \rangle. \quad (\text{S7})$$

The DIIS method relies on the property that a convergence condition is met when the single-particle correlation matrix commutes with the Fock matrix

$$F\Phi - \Phi F = 0. \quad (\text{S8})$$

This condition allows us to define an error vector for the n -th iteration as

$$\mathbf{e}_n = F_n \Phi_n - \Phi_n F_n, \quad (\text{S9})$$

where Φ_n is obtained from the diagonalization of F_n . The iteration process involves updating the Fock matrix as

$$F_k = \sum_{n=1}^{k-1} d_n F_n. \quad (\text{S10})$$

Here, d_n are the DIIS coefficients obtained through a least-squares constrained minimization of the error vectors. The aim of the optimization is to minimize the error given by

$$\text{Error} = \left| \sum_n d_n \mathbf{e}_n \right|^2 \quad (\text{S11})$$

with the constraint $\sum_n d_n = 1$. In our calculations, we set the convergent condition of the energy difference between two subsequent iteration processes as $10^{-8}t$.

ITINERANT FERROMAGNETISM AT ELECTRON DOPING $\delta = 1/2$

In the main text, we have presented key findings at electron doping $\delta = 1/2$. In this section, we provide additional numerical details and numerical data. For the convenience of readers, we also show the data presented in the main text to gain a complete picture of the evolution of magnetism when tuning the coupling strength U/t from finite to infinite U/t , as depicted in Fig. S2. These analyses reveal the emergence of itinerant ferromagnetism with increasing Coulomb interaction and enable a comprehensive understanding of the underlying mechanism under general interaction strength U/t .

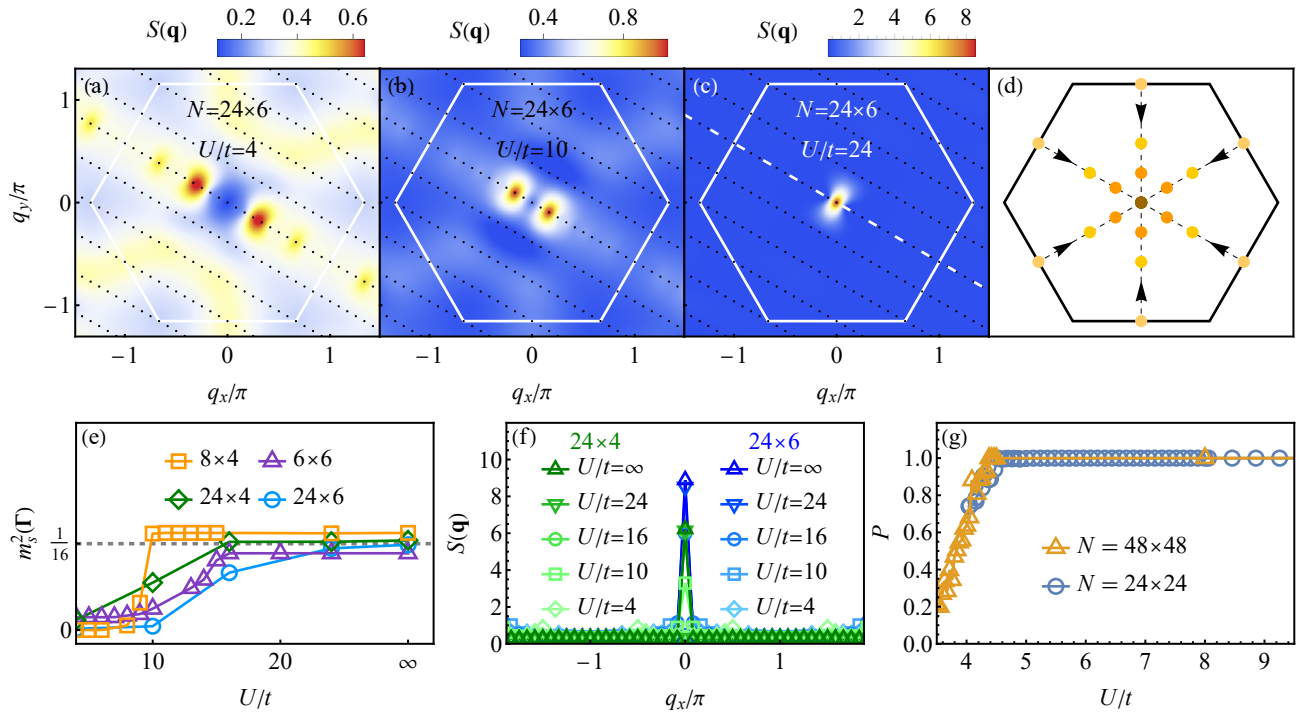


Fig. S2. The static spin structure factor $S(\mathbf{q})$ as a function of U/t at electron doping $\delta = 1/2$. (a)-(c) The contour plot of $S(\mathbf{q})$ for the $N = 24 \times 6$ system at $U/t = 4$ (a), $U/t = 10$ (b), and $U/t = 24$ (c). The black dots represent the accessible momenta in the Brillouin zone (denoted as a white hexagon), and interpolation has been applied in the contour plot. (d) Schematic of the evolution of the \mathbf{q}_0 with increasing U/t , indicated by the transition from lighter to darker colors following the black dashed arrows. Here, \mathbf{q}_0 denotes the momenta where $S(\mathbf{q})$ reaches its maximum, within the Brillouin zone represented by a hexagon. (e) Ferromagnetic squared order parameter $m_s^2(\Gamma)$ as a function of U/t . For larger U/t , the peak of $S(\mathbf{q})$ stabilizes at momentum Γ with a saturation value independent of N , indicating the fully polarized ferromagnetism. (f) Line-cut plot of $S(\mathbf{q})$ along the momentum path passing through the Γ point, depicted as a white dashed line in (c). (g) Polarization $P \equiv 2Nm_s(\Gamma)$ from the unrestricted Hartree-Fock method on $N = 48 \times 48$ and $N = 24 \times 24$ systems with periodic boundary conditions.

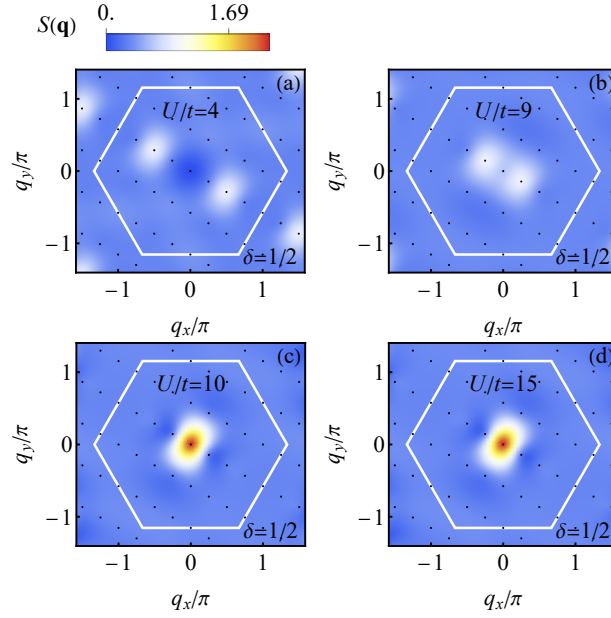


Fig. S3. (a-d) The contour plot of the static spin structure factor $S(\mathbf{q})$ across a range of U/t with $N = 8 \times 4$ at $\delta = 1/2$ for the Hubbard model.

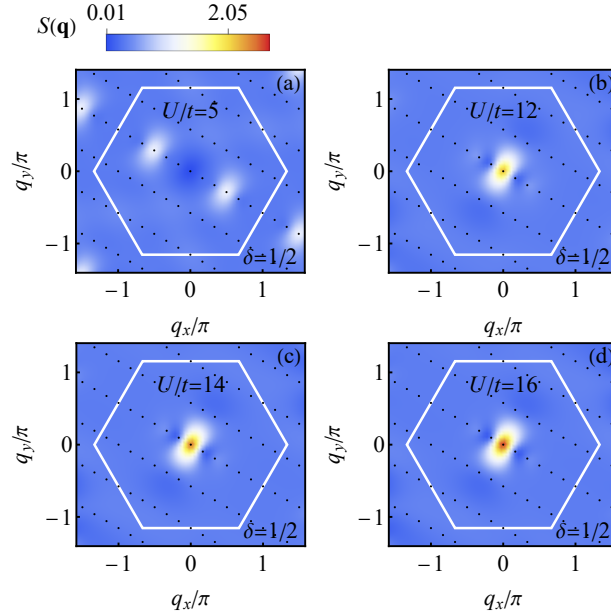


Fig. S4. (a-d) The contour plot of the static spin structure factor $S(\mathbf{q})$ across a range of U/t with $N = 12 \times 4$ at $\delta = 1/2$ for the Hubbard model.

The magnetic order is signaled by peaks at certain wave vectors $\mathbf{q} = \mathbf{q}_0$ in the static spin structure factor $S(\mathbf{q})$, defined by $S(\mathbf{q}) \equiv \sum_{\mathbf{i}, \mathbf{j}} \langle \mathbf{S}_{\mathbf{i}} \cdot \mathbf{S}_{\mathbf{j}} \rangle e^{i\mathbf{q} \cdot (\mathbf{i} - \mathbf{j})} / N$. We first focus on the evolution of the momenta \mathbf{q}_0 as a function of interaction strength U/t . For the noninteracting case ($U/t = 0$) in a triangular lattice, electron doping $\delta = 1/2$ corresponds to the Van-Hove filling at which a perfect nesting of the Fermi surface exists. In the weak-coupling limit $U/t \rightarrow 0$, it is expected that nesting leads to peaks of $S(\mathbf{q})$ locating at the \mathbf{M} points in the Brillouin zone. Previous weak-coupling theory proposes that the candidate ground state exhibits noncoplanar chiral magnetic order. When the weak coupling assumption is no longer applicable at intermediate to strong interaction strengths U/t , using DMRG we numerically observe that other magnetic ordering vectors distinct from the nesting vectors emerge, as shown in Figs. S2(a), (b) for $L_y = 6$. Interestingly, the locations of these peaks in $S(\mathbf{q})$ shift towards

the Γ point as U/t increases. Upon surpassing a critical strength U_c/t toward the limit $U/t = \infty$, the peak of $S(\mathbf{q})$ becomes fixed at Γ point, as illustrated in Fig. S2(c), (e), indicating the establishment of a stabilized ferromagnetic phase in the strong coupling regime. In Fig. S2(d), we schematically plot such evolution of the peaks in $S(\mathbf{q})$ with increasing U/t , as visualized by the dashed arrow from momenta \mathbf{M} to Γ . Notably, after the peak of $S(\mathbf{q})$ shifts to the Γ point, its height gets larger in a finite range of increasing U/t [see Fig. S2(f)], until reaching its maximum value and forming a plateau, as illustrated by Fig. S2(e). This signals the evolution from a partially-polarized to a fully-polarized phase. In particular, the saturated value matches the ferromagnetic squared order parameter $m_s^2(\Gamma) \equiv S(\Gamma)/N \sim \delta_{\mathbf{q},\Gamma}/16$ for a fully polarized state at electron doping $\delta = 1/2$.

We present additional supporting data for the evolution of the momentum \mathbf{q}_0 of the peak in $S(\mathbf{q})$ as a function of interaction strength U/t in Fig. S3 for $N = 8 \times 4$ and Fig. S4 for $N = 12 \times 4$. These results for $L_y = 4$ systems are consistent with the case of $L_y = 6$ in Fig. S2(a)-(c). The peak locations in $S(\mathbf{q})$ progressively shift toward the Γ point as U/t increases, as presented in Fig. S3(a-c) and Fig. S4(a,b). This observation supports the schematic plot in Fig. S2(d). After the peak of $S(\mathbf{q})$ shifts to the Γ point, its height increases within a specific range of U/t [see, Fig. S4(b-d)], until reaching its maximum value, as illustrated by Fig. S3(c,d) and Fig. S4(c,d), indicating a transition from a partially-polarized to a fully-polarized ferromagnetic phase.

The above numerical observations reveal the presence of ferromagnetism with increasing Coulomb interaction. To confirm its robustness in the thermodynamic limit, we further employ the unrestricted Hartree-Fock mean-field approximation (see details in Supplementary Materials Section). As shown in Fig. S2(g), the polarization $P \equiv 2Nm_s(\Gamma)$ increases gradually as U/t becomes larger, and finally a full polarization state occurs at $U \simeq 4.5t$ for both $N = 48 \times 48$ and $N = 24 \times 24$ systems under periodic boundary conditions on both directions. While disparities in polarization P between $N = 48 \times 48$ and $N = 24 \times 24$ lattice sizes are notable for $U \lesssim 4.5t$, beyond this threshold ($U \gtrsim 4.5t$) in the fully polarized ferromagnetic state, the polarization P shows minimal sensitivity to the size of the system. This echoes the observations in Fig. S2(e), suggesting the robust fully-polarized ferromagnetism regardless of system sizes in the strong coupling regime.

ITINERANT FERROMAGNETISM OF $t_{\text{QQ}} - U$ MODEL

The $t_{\text{QQ}} - U$ model is given by $H = H_{t_{\text{QQ}}} + H_{\text{int}}$, where the interaction term is the Hubbard repulsion $H_{\text{int}} = U \sum_{\mathbf{i}} n_{\mathbf{i}\uparrow} n_{\mathbf{i}\downarrow}$, and the projected hopping term is given by

$$H_{t_{\text{QQ}}} = - \sum_{\langle \mathbf{ij} \rangle, \sigma} t_{\text{QQ}} \hat{Q}_{\mathbf{i},\bar{\sigma}} c_{\mathbf{i},\sigma}^\dagger c_{\mathbf{j},\sigma} \hat{Q}_{\mathbf{j},\bar{\sigma}}. \quad (\text{S12})$$

Here, the projection operator is $\hat{Q}_{\mathbf{i},\sigma} \equiv n_{\mathbf{i},\sigma}$ and Eq. (S12) describes the NN hoppings between a doubly occupied site and a singly occupied site with hopping amplitude t_{QQ} [see Fig. 2(c) in the main text], i.e., the doublon-singlon exchange. In Fig. S5, we examine both the static spin structure factor $S(\mathbf{q})$ and electron momentum distribution $n(\mathbf{k})$ at electron doping $\delta = 1/2$ for $U/t = 10$, where the pronounced peak at Γ and the well-defined Fermi surface are consistent with the itinerant ferromagnetism observed in the Hubbard model at the same doping and the same coupling strength $U/t = 10$.

EVOLUTION OF MAGNETISM WITH DOPING FOR $L_y = 4$

In this section, we present the average spin correlations $\bar{S}(r=1)$ and the magnetic phase diagram as a function of U/t and electron doping δ specifically for $L_y = 4$. We also provide further data for $L_y = 6$ to enhance the comparison.

For the fully polarized phase of the Hubbard model with $U/t = 10$, $\delta \approx 1/2$, $L_y = 4$, the average spin correlations $\bar{S}(r=1)$ [yellow triangles in Fig. S6(a)] align well with those [blue circles] of the $t_{\text{QQ}} - U$ model Eq. (S12). This alignment underscores a deep connection between the ferromagnetic mechanisms inherent to both cases, and thus highlights the significant influence of doublon-singlon exchange in inducing ferromagnetism in the Hubbard model with finite U/t . In addition, for light electron doping around $\delta \approx 1/16$, the $\bar{S}(r=1)$ of the $t_{\text{QQ}} - U$ model [blue circles in Fig. S6(a)] closely matches with the fully polarized value (dashed black line) $m_{s,\text{F}}^2(\Gamma) \equiv [(1-\delta)/2]^2$, yet deviation becomes apparent around a doping range of $3/16 \lesssim \delta \lesssim 1/4$, the same as the ferromagnetic feature of the Hubbard model at $U/t = \infty$ for $L_y = 4$, as shown by the Fig. S6(b).

Figure S6(b) presents the magnetic phase diagram as a function of U/t and electron doping δ for $L_y = 4$, identifying two distinct ferromagnetic phases at $U = \infty$ around doping $\delta \approx 1/16$ and $\delta \approx 1/2$, separated by a doping range of $3/16 \lesssim \delta \lesssim 1/4$. The pattern of $S(\mathbf{q})$ at such separation [see Fig. S7(a)] is similar to that with finite U [see Fig. S7(c)], indicating that the iSDW at small doping extends from finite U to $U = \infty$ smoothly for the case of $L_y = 4$. This numerical observation suggests the subtle competition between the iSDW and FM at intermediate doping on narrower cylinders like $L_y = 4$ and the final stabilization of FM on wider cylinders like $L_y = 6$ [see Fig. 4(b) in the main text]. The notable separations of ferromagnetic phases around $\delta \approx 1/16$, $\delta \approx 1/2$ and $\delta \rightarrow 1$ for a finite system with $L_y = 4$ hint at diverse underlying mechanisms, potentially

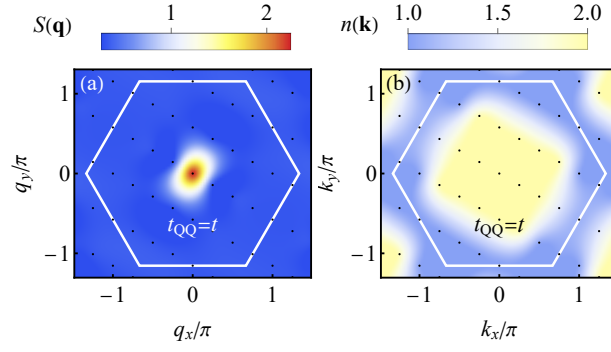


Fig. S5. Itinerant ferromagnetism signature for the $t_{QQ} - U$ model. (a) The static spin structure factor $S(\mathbf{q})$. (b) The electron momentum distribution $n(\mathbf{k})$. The black dots represent the accessible momenta in the Brillouin zone (white lines). Interpolation has been applied in the contour plot. Here, $N = 8 \times 4$, $U/t = 10$, $\delta = 1/2$.

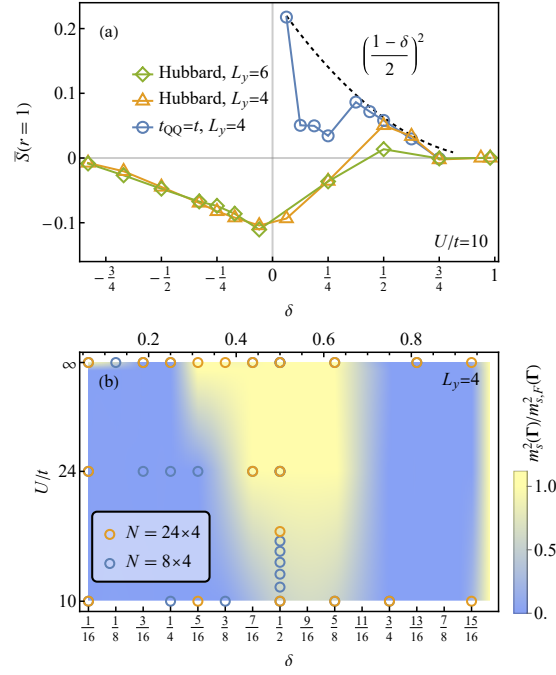


Fig. S6. (a) The average spin correlations $\bar{S}(r=1)$, as defined in the main text and indicated by yellow triangles ($L_y = 4$) and green diamonds ($L_y = 6$), are calculated across the nearest-neighbor bonds for the standard Hubbard model. These results are compared with those (blue circles) obtained when $t_{QQ} = t$ in Eq. (3) in the main text, with all other hopping processes absent. The dashed black line signifies the fully polarized case. The largest system sizes we presented here are $N = 16 \times 6$ and $N = 18 \times 4$ for 6- and 4-leg cylinders, respectively. (b) The renormalized ferromagnetic order parameter $m_s^2(\Gamma)/m_{s,F}^2(\Gamma)$ for the Hubbard model as a function of doping δ and interaction U/t . Here, $m_{s,F}^2(\Gamma) \equiv [(1-\delta)/2]^2$ corresponds to a full polarization value of $m_s^2(\Gamma)$. Circles denote the data obtained numerically.

differentiating the observed ferromagnetism around $\delta \approx 1/2$ from the Nagaoka ferromagnetism with $\delta \rightarrow 0$ and the Mielke's flat-band ferromagnetism or Müller-Hartmann ferromagnetism with $\delta \rightarrow 1$ for a finite size system, even though such separations of the ferromagnetic phases are absent for $L_y = 6$ [see Fig. 4(b) in the main text] at least for the largest length $L_x = 16$ that we have simulated. On the other hand, as the effective interaction U/t decreases from ∞ to $U/t = 10$ for $L_y = 4$, the ferromagnetic region around lighter ($\delta \approx 1/16$) and intermediate ($\delta \approx 1/2$) doping disappears and shrinks [Fig. S6(b)], respectively, yielding a ferromagnetic landscape closely aligned with the $U/t = 10$ case as depicted in Fig. S6(a). Additionally, for larger doping $5/8 \lesssim \delta < 1$, a distinct pattern in $S(\mathbf{q})$ indicates the presence of another iSDW phase [see Fig. S7(b,d)].

We further present the $S(\mathbf{q})$ outside the ferromagnetism phase at small doping with finite U and larger doping $5/8 \lesssim \delta < 1$ in Fig. S7. Our examination reveals two distinct features in $S(\mathbf{q})$, each indicative of a different iSDW phase.

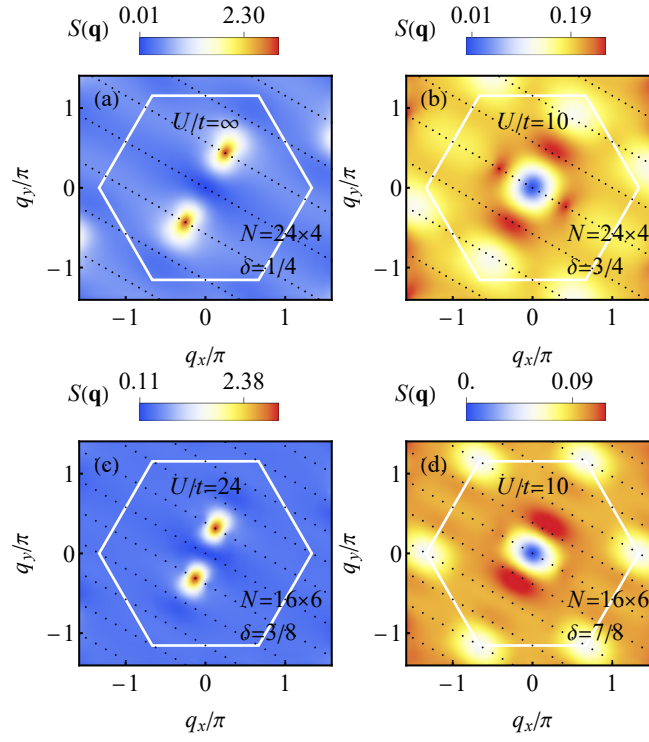


Fig. S7. Contour plots of the static spin structure factor $S(\mathbf{q})$ for the Hubbard model, illustrating two distinct iSDW phases. Panels (a) and (c) show phases at smaller doping, while panels (b) and (d) depict phases at larger doping.